Expanding Embedded 3D Bioprinting Capability for Engineering Complex Organs with Freeform Vascular Networks

Yongcong Fang[#], *Yihan Guo, Bingyan Wu, Zibo Liu, Min Ye, Yuanyuan Xu, Mengke Ji, Li Chen, Bingchuan Lu, Kaiji Nie, Zixuan Wang, Jianbin Luo, Ting Zhang, Wei Sun, Zhuo Xiong*[*]

Biomanufacturing Center, Department of Mechanical Engineering, Tsinghua University, Beijing 100084, P. R. China

Biomanufacturing and Rapid Forming Technology Key Laboratory of Beijing, Beijing 100084, P. R. China

"Biomanufacturing and Engineering Living Systems" Innovation International Talents Base (111 Base), Beijing 100084, P.R. China

E-mail: xiongzhuo@tsinghua.edu.cn

Abstract:

Creating functional tissues and organs in vitro on demand is a major goal in biofabrication, but the ability to replicate the external geometry of specific organs and their internal structures such as blood vessels simultaneously remains one of the greatest impediments. Here, we address this limitation by developing a generalizable bioprinting strategy of sequential printing in a reversible ink template (SPIRIT). We demonstrated that our microgel-based biphasic (MB) bioink can be used as both an excellent bioink and a suspension medium that supports embedded 3D printing due to its shear-thinning and self-healing behavior. When encapsulating human-induced pluripotent stem cells (hiPSCs), the MB bioink was 3D printed to generate cardiac tissues and organoids by extensive stem cell proliferation and cardiac differentiation. By incorporating MB bioink, the SPIRIT strategy enabled the effective printing of a ventricle model with a perfusable vascular network, which is not possible to fabricate using extant 3D printing strategies. Our SPIRIT technique offers an unparalleled bioprinting capability to replicate the complex organ geometry and internal structure in a faster manner, which would accelerate the biofabrication and therapeutic applications of tissue and organ constructs.

Keywords: Embedded 3D Bioprinting; Tissue Engineering; Microgel Assembly; Vascularization; Heart Chamber.

This article has been accepted for publication and undergone full peer review but has not been through the copyediting, typesetting, pagination and proofreading process, which may lead to differences between this version and the Version of Record. Please cite this article as doi: 10.1002/adma.202205082.

1. Introduction

In vitro replication of the complex structures and functions of human tissues and organs has long been a pursuit in the field of biofabrication[1]. Three-dimensional (3D) bioprinting technologies have attracted great interest for their capabilities to precisely deposit cell-laden hydrogels in a layer-by-layer fashion[2]. For most 3D bioprinting approaches (e.g., extrusion-based), a bioink needs to be smoothly extruded and then rapidly stabilized to maintain a printed structure while avoiding potential cell damage [3]. However, it is often challenging to print large free-form tissue structures owing to the inadequate structural integrity and mechanical stability of soft hydrogel-based bioink[4]. For the past decade, considerable effort has been made to address this particular challenge. For example, Kang and colleagues proposed a hydrogel reinforcing strategy by coprinting cell-laden hydrogel bioinks with synthetic poly-caprolactone (PCL) polymer that serves as a supporting framework[5]. Although this strategy allowed the fabrication of human-scale bone and cartilage tissue constructs, the mechanically robust PCL fibers often impeded the maturation of soft tissue such as the heart and liver. Alternatively, the embedded 3D bioprinting strategy has gained increasing popularity for constructing complex freeform structures[6]. In this approach, a suspension medium is utilized to support the deposition of bioinks in 3D space before cross-linking. The suspension medium undergoes rapid fluidization at yield stress and then solidification in the absence of stress due to its unique shear-thinning and self-healing properties[7]. The printed structures can easily be removed from the suspension medium by gently washing the suspension medium or raising the temperature. As an example of this strategy, Lee and colleagues printed a functional ventricle and full-size human heart model into a gelatin microparticles-based suspension medium by using a freeform reversible embedding of suspended hydrogels, also termed the FRESH technique[8].

Apart from the complex external geometry of native tissues and organs, another hurdle towards engineering large-scale functional tissues and organs is the lack of a hierarchical vascular network that facilitates the transport of nutrients and oxygen to maintain cell viability[9]. The sacrificial templating strategy has been widely employed to generate complex vascular networks within 3D tissue constructs[10]. For example, Lewis et al. printed sacrificial templates with predefined geometries using fugitive Pluronic F127 ink, which was subsequently cast with cell-laden hydrogels[11]. The 3D vascularized tissues (thickness ~ 1 cm) were generated by liquefying the sacrificial templates and seeding human umbilical vein endothelial cells (HUVECs) after printing and crosslinking. Multimaterial 3D bioprinting offers a more efficient strategy for producing vascularized tissues by simultaneously printing cell-laden bioinks and sacrificial bioinks[12]. For example, Dvir et al. printed a thick cardiac patch with vascular networks by alternately printing cardiomyocyte-laden decellularized extracellular matrix (dECM) and HUVEC-laden sacrificial gelatin bioinks in a layer-by-layer fashion[13]. It is noted that multi-nozzle 3D bioprinting fails to recapitulate the 3D complex geometries

of native vasculatures as the layer-by-layer deposition fashion often generates a planar lattice-like or woodpile arrangement[14].

For the past decade, the embedded 3D printing strategy has emerged to allow the omnidirectional printing of vascular networks with higher degrees of biomimicry[15]. The strategy explores the concept of printing a sacrificial bioink into a cell-laden suspension medium in an arbitrary manner rather than printing a cell-laden bioink into a sacrificial suspension medium. As an adaptation of this strategy, Skylar-Scott and colleagues introduced the sacrificial writing into functional tissue (termed SWIFT) technique, by developing a suspension medium that consists mainly of spheroids or organoids as organ building blocks (OBBs)[16]. The OBBs-based suspension medium possesses a unique shear-thinning and self-healing property that enabled the omnidirectional printing of sacrificial gelatin inks which, when removed, yielded perfusable vascular networks. SWIFT technique generates vascularized tissues with close to physiological cell density, however, it is unable to replicate the external geometry of native tissues and organs such as the heart chamber as the shape of the printed tissue is greatly restricted by the container. Therefore, there is a pressing need to bridge the gap between these two embedded 3D printing strategies, namely the FRESH technique and the SWIFT technique, to recapitulate the complexity of both external geometries and internal structures. The unbridged gap may be due, in part, to the lack of a cell-laden hydrogel or biomaterial which can serve as both a bioink and a suspension medium simultaneously for embedded bioprinting.

In this work, we address this unmet need by developing a novel bioprinting paradigm of sequential printing in a reversible ink template, also termed the SPIRIT technique. In contrast to conventional multi-nozzle 3D bioprinting, the SPIRIT technique includes several separate printing stages including the first printing of a bioink in a reversible suspension medium to generate the complex external geometry of native tissues and organs, the second printing of sacrificial ink into the freshly printed yet uncrosslinked constructs to generate a freeform vascular network, further in situ crosslinking, and the removal of suspension medium and sacrificial ink (Figure 1). The SPIRIT technique highly relies on developing a bioink that can serve as both a bioink and a suspension medium simultaneously. For that purpose, we used the cell-laden microgel-based biphasic (MB) bioink as reported in our previous work[17], which displayed a unique shear-thinning and self-healing over a wide temperature range and a fast in situ photocrosslinking capability. We demonstrated that the human-induced pluripotent stem cells (hiPSCs) laden MB bioink can be 3D printed with moderate cell viability, which could be further utilized to generate organ-specific tissues by extensive stem cell proliferation and differentiation. We successfully printed a ventricle model with a perfusable freeform vascular network by SPIRIT strategy using MB bioink, which is not possible to fabricate using extant embedded 3D printing strategies. We believe that the novel SPIRIT technique has the potential to revolutionize the paradigm of complex tissue engineering, accelerating the development of the biomedical applications of engineered tissues.

2. Results and Discussion

2.1. Characterization and 3D printing of cell-laden MB bioink

As previously reported[17], our MB bioink consists of microgels and a second hydrogel precursor. We first used a flow-focusing microfluidic device to generate microgels. Hydrogel precursor was injected into the microchannel and sheared by the continuous oil flow to generate droplets, which were further crosslinked. After crosslinking, microgels were rinsed with phosphate buffer saline (PBS) to remove excess oil and surfactant (Figure 2a). These microgels exhibited a very uniform size distribution of ≈ 215 μm with a coefficient of variation (CV) of less than 2.5% (Figure 2b). In contrast to other techniques such as batch emulsion[18], lithography[19], and electrohydrodynamic (EHD) spraying[20], microfluidics offers excellent control of microgel geometries and sizes by designing the microfluidic channels and tuning flow rates (Figure 2c). As previously reported[21], microgels could be jammed through centrifugation or vacuum filtration to further remove the aqueous medium between them. Centrifugation is preferred in the presence of cells that are more viable[22]. We blended the compacted microgels with the other hydrogel precursor and centrifuged them to remove excess fluid. The process was repeated several times, resulting in the MB bioink (Figure S1). We were able to control the void space between microgels by adjusting the centrifugation force and duration.

MB bioink demonstrated excellent printability with a regular filament extended vertically 5 cm without breaking (Figure 2d). The MB bioink can easily be printed into various constructs (Figure 2e). This is due to the unique shear-thinning, yielding, and self-healing properties. MB bioink provides a protective microenvironment from shear stress during printing or injection, which is beneficial for cell viability. In addition, MB bioink creates a heterogeneous cellular microenvironment at the microscale, which facilitates vascularization and tissue function. In this study, we explored the printing of human-induced pluripotent stem cells (hiPSCs) capable of self-renewal and differentiation into multiple cell types[23]. Due to their sensitivity to extrinsic physical signals, hiPSCs were encapsulated within gelatin/alginate microgels rather than GelMA microgels, which depended on free radical polymerization. The free-radical polymerization is notoriously cytotoxic and hinders the translation of the MB bioink to *in vivo* applications[24]. The hiPSCs-laden gelatin/alginate microgels were double crosslinked by calcium ionic crosslinking and enzymatic crosslinking with microbial transglutaminase (mTG). Alginate forms an instant and reversible network via ionic bonding with calcium ions, while mTG forms covalent bonds between glutamine and lysine residues of gelatin. The hiPSCs within gelatin/alginate microgels exhibited moderate viability of 69.5%±11.0% due to the mildness of the enzymatic and ionic reactions (Figure 2f). The hiPSCs-laden microgels were further blended with the same gelatin/alginate hydrogel precursor to generate an MB bioink (Figure 2g). After printing and

crosslinking, the viability of hiPSCs within the printed filaments decreased to 45.8%±6.4% (Figure 2h), indicating that shear forces during printing negatively affected cell viability. Additionally, the initial cell viability of cell-laden bioink could be further improved by optimizing the microgel fabrication process. In future work, we plan to use vegetable oil which contains antioxidants to avoid cell damage exposed to mineral oil.

During the culture period, hiPSCs continued to proliferate and tended to grow as cellular aggregates, also known as embryoid bodies (EB) (Figure 2i). The diameters of the EBs increased with culturing time (Figure 2j). Most of the EBs were contained in the printed filaments throughout the culturing period (Figure S2), which displayed a rapid proliferation rate (15-fold within 7 days) indicated by the OD value (Figure 2k). On day 8, more than 85% of the EBs were stained with pluripotency markers Oct4 and Nanog using immunofluorescence staining (Figure 2l) and flow cytometry analysis (Figure 2m), validating pluripotency maintenance of hiPSCs. These EBs mimicking the specific structure of the developing embryo are beneficiary in the initiation of differentiation towards many lineages such as cardiac cells [25]. After switching the mTeSR1 media to the cardiomyocyte differentiation medium on day 8, cardiac differentiation from EBs-laden MB bioink was initiated (Figure 2n). After 14 days of cardiac differentiation, beating cardiac organoids were observed (Figure 2o, Movie S1), suggesting that an in situ expansion and differentiation of hiPSCs-laden MB bioink can be explored to generate organ-specific tissue.

2.2. Embedded bioprinting of MB bioink for engineering complex constructs

We explored the embedded 3D bioprinting of MB to engineer more complex tissues and organs. One of the key elements in embedded bioprinting is the suspension medium that can support the deposition of bioink during printing. For that purpose, we developed two types of granular suspension media consisting of either commercially available Carbopol (Figure S3) or gelatin microparticles (Figure S4), which are both widely used in embedded bioprinting. Carbopol-based suspension medium consists of polyacrylic acid-based microgels with diameters less than 7 μm[26]; while gelatin microparticles-based suspension medium consists of irregular gelatin particles with diameters ranging from 20 μm to 30 μm[27]. Both suspension media possess shear-thinning and self-healing properties. The Carbopol-based suspension medium has the advantage of providing optical imaging and in situ measurement; however, the gelatin microparticle-based suspension medium has the advantages of biocompatibility and is easy to remove by raising the temperature. To enable photocrosslinking of the printed constructs without modifying the suspension medium, we used an MB bioink consisting of GelMA microgels and GelMA precursors for SPIRIT as a proof of concept.

We printed the MB bioink containing red dyes in a zigzag pattern to illustrate the printing accuracy (Figure 3a). From our experimental experiences, GelMA MB bioink at lower temperatures tends to

form buckling of filaments, whereas GelMA MB bioink at higher temperatures tends to diffuse away after deposition. We evaluated the impact of printing temperature on printing accuracy by using a parameter referred to as structural similarity index (SSIM), adapted from the previous work of Burdick and colleagues[28]. We measured the index by comparing the images of the printed filaments and ideal print designs using the Python program (Figure 3b). Images of prints were converted to binary images, segmented, and analyzed to determine average filament width and SSIM. Increasing the printing temperature resulted in a widening of the filaments, and SSIM was highest at 24°C (Figure 3c,d). The diameters of the printing filaments can be fine-tuned by controlling the extrusion rate at a constant printing speed (Figure 3e). In this study, most embedded printing used a printing speed of 3 mm/s and an extrusion rate of 0.4 μL/s.

Further, we explore the embedded bioprinting of MB bioink to create highly complex tissue constructs for potential biomedical applications. We printed a full heart model (Figure 3f-g), open chamber (Figure 3h-i, Movie S2), and bronchus model (Figure 3j-k) in a Carbopol-based suspension medium as representative examples as they encompassed geometrical features such as overhangs and cavities, which is often challenging for 3D direct bioprinting with hydrogel-based inks[29]. The printed open chamber was filled with blue ink without leakage (Figure 3i), suggesting there was close interconnectivity between filaments in all directions. It should be noted that the bronchus model with hollow branches and thin walls was embedded 3D printed in the "top-down" approach rather than in the "bottom-up" approach in our previous work. We compared the printing accuracy between 3D direct printing and embedded printing by quantitatively evaluating the shape fidelity of the printed tubular structures with the same print design (Figure 3l-m). Upon photo-crosslinking, the samples were removed from the suspension medium by dilution. The outer diameter (O.D.) and height of embedded printed structures were slightly higher than the input values, while these dimensions of directly printed samples were marginally lower than the inputs (Figure 3n). This is probably attributed to the less compacted connection of filaments in the presence of a suspension medium.

Previously, we reported that the MB bioink exhibited hyperelasticity with excellent cyclic compression and stretch endurance after 3D printing[17]. We further evaluated the mechanical performance of embedded printed constructs by subjecting them to cyclic stretching (Figure 3o-p, Movie S3). The constructs could undergo ~40% strain and recover elastically, thus validating their mechanical robustness due to a mechanical fusion between the printed layers. Additional mechanical characterization was performed by creating cast and 3D printed solid cylinder structures using MB bioink and subjecting them to uniaxial compression testing to generate stress-strain curves, with the linear region from 5 to 20% strain used to calculate the elastic modulus (Figure 3q). The embedded printed samples had an elastic modulus of 8.55 ± 2.21 kPa, about two times that of the cast samples (4.59 ± 0.60 kPa) (Figure 3r); however, the cast samples had stress to failure of 236.96 ± 2.67 kPa,

about three times that of embedded printed samples (85.06 ± 6.04 kPa). Part of this difference is because the embedded printed samples could not reach 100% infill, which would inevitably introduce internal voids or residual Carbopol medium that initiated cracks at higher strains. However, these results, in combination with the straining of the embedded printed tubular structures, demonstrated the mechanical fusion between printed layers and showed that embedded 3D printing of MB bioink can be used to fabricate soft structures with structural integrity.

Cell viability after embedded 3D printing was assessed by performing a Live/Dead assay on prints with GelMA MB bioink containing HepG2 cells (Figure 3s,t). Commonly used GelMA bioink with HepG2 cells was directly printed into mesh-like structures as a control. The cell-laden microgels were well distributed in 3D filaments with viability of 68.7%±7.2%, relatively lower than the viability of GelMA bioink (89.2%±3.3%) (Figure 3u). The lower cell viability of the embedded prints with MB bioink was expected because of the detrimental effect caused by the MB bioink preparation process and the Carbopol-based suspension medium in addition to the shear stress during printing. Despite their initial lower viability, the HepG2 cells within the embedded printed samples exhibited a faster growth rate in the first 5 days over in vitro culturing (Figure 3v).

2.3. Freeform vascular printing using MB bioink as a suspension medium

Granular hydrogels have been widely reported to be an ideal medium that supports the embedded printing of three-dimensional structures with arbitrary design[30]. This is because that granular hydrogel consisting of microgels ranging from 1 μm to 1000 μm possesses the unique rheological properties of shear-thinning and self-healing, also known as jamming/unjamming transition. As previously reported, our MB bioink composed of cell-laden microgels has granular characteristics that permit recoverable yielding[17]. Therefore, our MB bioink has the potential to serve as a suspension medium that supports embedded 3D printing. To demonstrate this, MB bioink was transferred into a transparent container and further compacted, in which patterned filaments made of sacrificial gelatin ink were successfully embedded (Figure 4a). The printed filaments retained a close to the cylindrical profile at varied extrusion rates as shown by the optical images at the cross-section (Figure S5a,b). The cross-section areas of the printed filaments scaled linearly with the extrusion rates (Figure S5c), following the principle of volume conservation. Further, we calculated the equivalent widths of the printed filaments using ImageJ software. As shown by the fitted line, these filament widths scale with the square root of the extrusion rates (Figure S5d). Therefore, the filament widths can be easily tuned from 250 μm to 1000 μm by changing the extrusion rates (Figure 4b,c).

In the previous work of Skylar-Scott and colleagues[16], the OBB-ECM slurry had to be held at 2°C during printing so that the highly temperature-dependent collagen/Matrigel solution exhibited the requisite self-healing, viscoplastic response to enable the embedded printing. Similarly, ECM-derived

GelMA hydrogel possesses an inherent temperature-dependent sol-gel transition, originating from the triple helix formation of denatured collagen fibers (i.e., gelatin). For example, the sol-gel transition temperature of 5.0 wt% GelMA bulk hydrogel is appropriately 18.5 °C; however, the GelMA MB bioink was maintained in the gelled state (i.e., storage modulus (G′) >loss modulus (G″)) across the temperature range of 4~37 °C (Figure S1c). Therefore, in this study, the embedded printing was compatible with MB bioink at wider temperature ranges due to their less temperature-dependent rheological properties, which is beneficial for biomedical applications in different clinical settings especially when temperature control is impractical. Although GelMA MB bioink is much less temperature sensitive than GelMA bulk hydrogel, the shear moduli of MB bioink decreased with increasing temperature, suggesting that the printing fidelity is still partly affected by temperature change as shown in Figure 4d and Figure S6.

By writing sacrificial ink into the MB bioink, we were able to create perfusable tissue constructs. Adapted from the work of Skylar-Scott, we first created a custom-shaped transparent mold (5 mm thick) with a single inlet and outlet for perfusion and filled it with 3 ml of compacted MB bioink. Here, we designed and printed a bifurcated channel (Figure 4e) by learning from nature. After printing, the MB bioink-based suspension medium was photo-crosslinked (Figure 4f,g), and the sacrificial gelatin was removed by raising the temperature to 37℃ to generate channels. The resulting channels were further perfused with blue ink to prove their perfusability (Figure 4h, Movie S4). HepG2 cells at a high density of 4×10^7cells/ml were encapsulated within the GelMA microgels (Figure S7a). We further prepared HepG2-laden MB bioink and printed perfusable channels within the hepatic tissues. The initial cell viability of HepG2-laden MB bioink was appropriately 90% (Figure 4i). After perfusion culture for 18 hours, the tissue constructs were removed from their perfusion chambers. Their high cell density made it difficult to image the core of individual microgels within these matrices. Therefore, we manually sliced the tissue constructs into 1–2-mm-thick sections with a microtome blade and stained them with Calcein AM/PI staining kit to assess their cell viability. We found that luminal perfusion of the perfusable MB bioink-based hepatic tissue greatly enhanced cell viability throughout the bulk tissues (Figure 4j, Figure S7b,c). Moreover, cells in an annular zone in close proximity to the perfused channel maintained their high viability, whereas viability elsewhere was attenuated after 18 hours (Figure S7d-f). These trends are consistent with previous viability data and mathematical models of oxygen diffusion and consumption[31], indicating that the cells closest to the channel consume most of the oxygen, thereby forming a characteristic viability depth (i.e., the Krogh radius). Taken together, these results demonstrated that such tissue perfusion translates into higher tissue viability.

By using a HUVEC-laden sacrificial gelatin bioink, we were able to introduce the formation of endothelial-lined channels within these constructs made of MB bioink. As previously reported[32], the

in situ endothelialization strategy can generate a more uniform EC distribution throughout the channels compared to the post-EC seeding strategy. Specifically, the sacrificial gelatin bioink was loaded with HUVECs at a density of 10^7 cells/ml, and embedded 3D printed in the MB bioink-based suspension medium. After printing and photo-crosslinking, the encapsulated HUVECs were released by liquefying the gelatin filaments at 37℃. The cells were allowed to adhere to the luminal surface uniformly by flipping the printed constructs every 30-60 min. The constructs were further connected with an inlet and outlet tube for perfusion to remove the gelatin and any nonadhered cells. On day 3, we observed the HUVECs uniformly distributed throughout the templated channels (Figure 4k). On day 7, the cells appeared to proliferate to form a homogenous, confluent endothelial layer in the channels (Figure 4l). Moreover, we observed HUVEC invasion into the surrounding matrix (Figure 4m). Furthermore, we printed MB bioink (stained with red dye) into a suspension matrix of transparent MB bioink with smooth extrusion and good fidelity (Figure 4n-o). Red and green fluorescent GelMA microgels were used for the ink and suspension medium to help visualize the distribution of printed bioink (Figure 4p). These results provide more convincing evidence that MB ink is capable of acting as both an ink and an embedded printing matrix.

2.4. Principle and characterization of SPIRIT printing

Encouraged by the excellent rheological properties of our MB bioink, we developed a novel bioprinting paradigm by sequential printing in reversible ink template strategy (SPIRIT technique). The SPIRIT technique includes several separate printing processes as follows: i) First printing: we print MB bioink into a Carbopol or gelatin microparticles-based suspension medium to generate complex external structures such as chambered ventricles; ii) Second printing: upon the completion of the first printing process, we print a sacrificial ink such as P-F127 or gelatin into the freshly printed yet uncrosslinked constructs to generate a freeform vascular network by capitalizing the reversible self-recovery behavior of MB bioink; (iii) Crosslinking: we crosslink the printed tissue constructs by in situ photo-crosslinking or incubation at 37℃ while retaining the structural integrity of printed constructs in step (i) and (ii). (iv) Removal of suspension medium and sacrificial ink: We remove the printed constructs from the suspension medium by temperature changing or dilution while the sacrificial ink can be removed simultaneously or separately (Figure 5a). Compared with current 3D bioprinting strategies[33], the SPIRIT technique has the potential to create tissues and organs with extraordinary complexities in both external geometries and internal structures. However, the major challenge of the SPIRIT strategy lies in the design and control of MB bioink to ensure a smooth first printing and second printing that would not agitate the printed patterns. On one hand, after deposition into the suspension medium, MB bioink should maintain its original rheological behavior, especially the self-healing, viscoplastic response to enable a subsequent sacrificial ink writing. This implies that

any spontaneous stiffening or thermal gelation of the MB matrix within the suspension medium should be avoided during the SPIRIT printing process. On the other hand, after the second printing, the MB bioink should be capable of undergoing in situ or remote crosslinking so that the printed constructs can be stabilized before being extracted from the suspension medium (Figure 5b).

Following these criteria for SPIRIT printing, we used GelMA MB bioink at the concentration of 5wt% and 7.5wt%, respectively. GelMA MB bioink can be remotely stabilized via photo-crosslinking in addition to its shear-thinning and self-healing properties. Although GelMA is highly temperature-sensitive, our GelMA MB bioink possessed much less temperature-dependent rheological properties. We used a Carbopol-based suspension medium and sacrificial gelatin bioink (7.5wt%) that contained red dye to demonstrate the SPIRIT printing process. During the first printing stage, both 5% and 7.5wt% GelMA MB bioink were smoothly printed into tubular constructs in a Carbopol-based suspension medium; However, in the second printing stage, during the sacrificial writing of helical filaments, the syringe needle tended to drive the first printed constructs moving and rotating when using 7.5% GelMA MB bioink (Figure 5c, Movie S5) while the movement of the first printed constructs made of 5wt% GelMA MB bioink was less evident (Figure 5d, Movie S6). Part of this difference is because the shear yield strain (~105%) of the 7.5% GelMA MB bioink is much higher than that of the suspension medium (~ 71%) while the shear yield strain (~38%) of the 5% GelMA MB bioink is considerably lower (Figure 5e,f). Experimentally, we found that the relative movement between the MB bioink and the suspension medium was much less during the second printing stage when the shear yield strain of the MB bioink is much less than the suspension medium, allowing the MB bioink to accommodate nozzle translation.

We successfully SPIRIT printed a tubular structure embedded with helical filaments using 5wt% GelMA MB bioink (Figure 5g,h), which was perfused by a culture medium containing blue dye (Figure 5i) upon removal of the suspension medium and sacrificial ink. The dimensions of the helical channel were close to the print design, indicating a good fidelity of SPIRIT printing (Figure 5j). Multiple constructs exhibited very similar dimensions with CV less than 2.5% (Figure S8), suggesting a high reproducibility of SPIRIT. We noted that the height and O.D. of the tubular structures slightly increased (less than 3%) after the second printing due to the embedding of sacrificial ink (Figure 5k). We calculated that the volume of embedded helical fibers was only equivalent to 1.57% of the printed tubular structure in the first printing stage. In most tissues and organs of the human body, blood vessels only occupy a relatively small volume[34]; as a result, the increase of printed constructs is marginal when SPIRIT printing is used to create human tissues and organs, especially with complex vascular geometry. However, the impact of second printing on the final printed structures would be non-negligible when we SPIRIT print tissue constructs embedded with larger internal structures.

Therefore, our ongoing efforts are focused on quantifying the impact and developing a counter-compensation approach in future work.

Printing time is a critical parameter that directly impacts the viability of the encapsulated cells, especially in the generation of large complex tissue constructs. In addition to the ability to create complex tissues/organs with the freeform vascular network, the SPIRIT technique has another advantage of fast printing speed compared to the conventional multi-nozzle bioprinting strategy as a vascular curve is extruded continuously rather than in a typical layer-by-layer fashion. For the construction of a tubular construct with a helical vascular network (height of 12 mm, O.D. of 16 mm, I.D. of 10 mm) as an example, it took 60min26s and 65min16s for SPIRIT printing (Movie S7) and conventional multi-nozzle printing strategy (Movie S8) at the same printing parameters, respectively; however, it took as much as 58min43s to finish the first printing of the tube. Therefore, it took much less time to generate a vascular network within the tubular structure for SPIRIT printing (i.e., 1min43s) than the conventional multi-nozzle printing strategy (i.e., 6min33s) (Figure S9) by saving the time of switching nozzle. It should be noted that the advantage of printing speed would be more significant when the vascular network becomes more complex.

2.5. SPIRIT printing ventricles with freeform vascular networks.

Our primary motivation for developing the SPIRIT technique is to enable the 3D printing of tissues and organs with complex external geometry and internal structures. The vascularized ventricle model serves as a good example to demonstrate the printing capabilities of the SPIRIT technique as the heart is a hollow chambered organ with a very dense vascular network to satisfy its high oxygen demand[35]. However, so far, current embedded 3D bioprinting strategies have failed to replicate the geometries of multi-chamber and vascular networks simultaneously. First, we created a simplified ventricle model with a diameter of around 2 cm and a wall thickness of around 4 mm. By using the Geomagic Wrap software, we designed a hierarchical vascular network (Figure 6a,b) located at the middle surface of the ventricle model, which occupied only 3.5% of the ventricle, respectively. We used the Carbopol-based suspension medium to visualize the SPIRIT printing process (Movie S9). After the first printing of the ventricle constructs using MB bioink (Figure 6c), we continued to print red dye-containing gelatin ink to generate vascular networks (Figure 6d-f). During the second printing stage, we tuned the diameters of each branch by controlling scan times or changing the extrusion rates at constant print speed. We successfully printed a ventricle construct embedded with a hierarchical vascular network, which demonstrated good coregistration of primary features when overlaid with the 3D model (Figure 6g-h). It should be noted that the printing order of the vascular network needs to be carefully assigned from bottom to top. By doing so, we can avoid the nozzle translating through previous features printed by sacrificial gelatin ink, otherwise, it would inevitably agitate or destroy the

printed patterns. After the removal of the suspension medium and sacrificial ink, the entire hierarchal vascular network within the printed ventricles could be repeatedly perfused by connecting with a syringe pump (Figure 6i,j, Figure S10, and Movie S10).

To fully leverage the newfound printing capability of SPIRIT, we seek to design and fabricate a more complex, perfusable vascular network that could densely fill the ventricle model. Here we first design a dendritic vascular network in 2D by using a mutual tree attraction algorithm adapted from previous work[36]. The vascular network was further curved to fit within the ventricle model (Figure 6k, Figure S11), resembling the vascular tree morphology of the coronary artery. Oxygen transport simulation revealed the inclusion of a dense vascular network greatly improved the oxygen transfer efficiency (Figure 6l, Figure S12). As shown in Figure 6m-n, we successfully printed a dense vascular network with 3D tortuosity and varying diameters. We observed that the chamber geometry of the printed ventricles remained intact even though they had been sheared by the shaft of the printing nozzle hundreds of times. This is attributed to the excellent self-healing behavior of the MB bioink. A distance map from the overlaid template and the final printed structures was generated (Figure 6o), and the fraction of voxels of the printed structure within 0.5 mm of the template was found to be more than 95.0%, showing a high shape fidelity of SPIRIT printing. Similarly, the same ventricle with an internal vascular network was also SPIRIT printed in a gelatin microparticle-based suspension medium (Figure S13-14, Movie S11). A single layer of vascular network may not be enough to satisfy the metabolic demand of a ventricle model as thick as 4 mm due to the limited diffusion distance of printed channels. Therefore, a multi-layer vasculature, the printing paths of which should be well designed to avoid potential interference, is highly required to improve the overall perfusability of SPIRIT printed ventricles. Currently, capillaries at the size of several microns are too small to be printed by SPIRIT. In future work, we may be able to generate a hierarchical vasculature with close to physiological vessel density by using a MB bioink conducive to vascularization by endothelial cell assembly for SPIRIT. In additional to the ventricle, we generated a simplified liver model with arbitrary vascular networks by SPIRIT, whereby fugitive Pluronic F-127 was used as an alternative sacrificial ink for its temperature-dependent phase behavior (Figure S15).

As a final demonstration, we assessed the viability of a scaled ventricle construct with perfusable vascular networks (Figure 6p). We prepared the cardiomyocytes-laden MB bioink using neonatal rat ventricular cardiomyocytes (NRVCs) because they are high-quality primary myocyte cells prepared by standard methods, and are ready for immediate use. Upon isolation, the NRVCs were embedded within GelMA microgels and further prepared into MB bioink for SPIRIT printing (Figure S16). As the printed ventricles were out of focus of a confocal microscope, we cut the printed ventricle into several pieces and used confocal imaging to gain the structural (e.g., channels) and cellular (cell distribution and viability) information (Figure 6q, Figure S17a-b). As demonstrated by Live/Dead

staining (Figure 6r-s; Figure S17-18), the printed vascular network greatly promoted the viability of the printed tissues during in vitro culture. A time-lapse microscopy visualization revealed the functional calcium handling of the printed tissues on day 10 (Figure 6t, Movie S12). The immunofluorescent staining (Figure 6u) confirmed the presence of sarcomeres and cellular interconnection, suggesting the preliminary maturation of the printed ventricles. These results revealed the proper functionality of the printed tissues, which demonstrated the feasibility and utility of SPIRIT in biomedical applications such as organ printing. Currently, the viability in SPIRIT is still a substantial limitation as it requires an additional harsh preparation process of MB bioink, which involves at least: a) droplet formation by shear forces applied by continuous phase fluid (i.e. mineral oil), b) microgel stabilization by in situ crosslinking, and c) oil removal by repeated rinsing process. In future work, we should optimize the preparation process and material component for MB bioink to improve its initial viability prior to SPIRIT. Furthermore, we envision that the SPIRIT strategy can work as a generalizable printing paradigm by incorporating a variety of bioinks with self-thinning and self-healing properties such as the supramolecular hydrogels developed by Burdick and colleagues[37], and OBB-ECM material developed by Skylar-Scott and colleagues[16, 38]. Our ongoing efforts are focused on incorporating high-density spheroids-based bioink with the SPIRIT strategy to achieve close to physiological cell density while maintaining the printing capability of SPIRIT. With its flexibility in materials and architectures, the SPIRIT technique provides a new level of capability in the fabrication of complex organs for regenerative applications and complex multi-material constructs for biomedical applications.

3. Conclusion

In summary, we introduce the concept of the SPIRIT printing strategy based on the MB bioink, which was demonstrated to serve as both an excellent bioink and a suspension medium simultaneously for embedded bioprinting. When encapsulating hiPSCs, the MB bioink could be printed into organ-specific tissues by extensive stem cell proliferation and differentiation. As an exemplar, we successfully printed a ventricle model with a freeform vascular network, which was perusable to increase the oxygen transport efficiency and thus the cell viability. We demonstrated that the SPIRIT technique is well compatible with the current suspension media (Carbopol or gelatin microparticles) and sacrificial inks (gelatin or Pluronic F127). While we have presented an extensive study of the SPIRIT printing using the MB bioink, this printing approach should be generalizable to other hydrogels with self-thinning and self-healing properties such as the supramolecular hydrogels. This SPIRIT approach offers an unparalleled bioprinting capability wherein complex tissue constructs with an embedded internal structure such as a freeform vascular network can be easily created with much less printing time. Looking forward, we can leverage these SPIRIT bioprinting capabilities to

engineer complex tissues and organs and accelerate important breakthroughs in biofabrication and tissue engineering for therapeutic applications.

4. Experimental Section

Materials: GelMA hydrogels with a methacrylate degree of 60% were purchased from EFL Inc., China. Red and green fluorescence-conjugated GelMA hydrogels were used for the visualization of the MB bioink. Carbopol-based suspension medium was purchased from SunP Inc., China. Alginate and gelatin were purchased from Sigma Aldrich and used as supplied.

Cell line culture: C2C12 and HepG2 cells were purchased from China Infrastructure of Cell Line Resources. C2C12 cells were cultured in Dulbecco's Modified Eagle Medium (DMEM, Thermo Fisher) supplemented with 10% fetal bovine serum (FBS, Biological Industries), 1% penicillin/streptomycin (P/S, Life Technologies), and 1% MEM Non-Essential Amino Acids (NEAA, Life Technologies). Similarly, HepG2 cells were cultured in Gibco Minimum Essential Media (MEM, Thermo Fisher) supplemented with 10% FBS and 1% P/S. HUVECs were purchased from American Type Culture Collection (CRL-1730, ATCC) and cultured with a cell growth medium from Lonza (CC3126). Cells were collected by digesting with 0.05% Trypsin/ethylenediaminetetraacetic acid (EDTA) (Life Technologies) and automatically counted using a cell counter (Countstar, China) before being encapsulated within a hydrogel precursor solution. C2C12 cells were transduced with retroviral vectors encoding green fluorescence protein from Hanhen Inc. to illustrate the cellular distribution within MB bioinks.

Human iPSCs culture and cardiomyocyte differentiation: Human iPSCs were purchased from American Type Culture Collection (ACS-1031, ATCC) and cultured under a feeder-free condition with mTeSR™1 medium (STEMCELL Technologies) refreshed daily. Cells were passaged weekly by dissociating with 2ml of ReLeSR™ followed by mechanical trituration. Cells were replated on the 6-well plate pre-coated by Matrigel (BD), diluted to 250 μg mL^{-1} in Dulbecco's modified Eagle medium (DMEM)/F12 (Thermo Fisher). The cardiomyocyte differentiation was performed according to the protocol of STEMdiff™ Cardiomyocyte Differentiation Kit (STEMCELL Technologies). Briefly, after the removal of the iPSCs culture medium, cells were washed twice with DPBS solution, and the full medium was replaced every other day by Medium A on day 2, Medium B on day 4, Medium C on day 6 and day8, and Maintaining Medium till day 14.

Isolation and culture of neonatal rat ventricular cardiomyocytes (NRVCs): Cardiomyocytes were harvested from neonatal rat hearts according to the ethical use protocols of Tsinghua University adapted from previous literature[10]. Briefly, the ventricle tissues were isolated from the rat hearts, minced, and digested in a 0.05% (w/v) trypsin solution without EDTA at 4℃ overnight. After trypsin digestion, cells were serially digested using 1 mg/ml type II collagenase solution (Worthington

Biochemical Corp.) until dissociated into a single-cell suspension. Dissociated cells were collected, filtered with a 100 μm strainer, and centrifuged at 1200 rpm for 3 min to yield the cell pellets. The isolated cells were plated and incubated for 45 min in tissue culture flasks. The non-adherent cardiomyocytes were resuspended, harvested, and cultured in DMEM supplemented with 10% FBS and 1% P/S.

Microgel generation: Microgels were generated using the PDMS-based single-channel microfluidic devices as previously described[17]. Briefly, polydimethylsiloxane (PDMS; Sylgard 184, Dow Corning) was cast onto a SU-8 resin mold fabricated via stereolithography. After curing at 70 °C for 1 hour, the PDMS substrate was peeled off, punched with 0.75 mm diameter biopsy punches to create inlet and outlet channels, cleaned with double tape, and plasma-bonded to a standard glass slide. Silicone tubing was inserted into the inlet and outlet channels. To generate microgels, light mineral oil (Sigma) with 2 v/v % Span 80 was used as the continuous phase with a flow rate of 4 mL/hr, and polymer precursor solution was used as the dispersed droplet phase with a flow rate of 0.75 mL/hr. For gelatin/alginate composite microgels, the droplets were first crosslinked by cooling outlet tubing and a collecting reservoir at 4 ℃, followed by immersing in calcium chloride solution. For GelMA microgels, the droplets were exposed to visible light (405nm, ~40 mW/cm^2) for 30 s ~ 60 s. All the microgels were suspended in PBS solution and centrifuged at 1000 rpm for 3 min, and the oil layer on top was aspirated. The rinsed microgels in PBS were stored for several hours before use. The diameter distribution of microgels was analyzed using ImageJ software (NIH).

MB bioink preparation: MB bioink was prepared as previously described[17]. Briefly, the collected microgels in PBS were centrifugated to remove extra fluids. The packed microgels were blended with a second polymer precursor solution, and centrifugated to remove the extra fluids on top. The process was repeated thrice so that the inter-microgel space was replaced by the second hydrogel phase. To visualize the composition of MB bioink, red and green fluorescein-conjugated GelMA hydrogels were used as the microgel phase and hydrogel phase, respectively. 3D printed filaments containing fluorescent MB bioink were visualized using confocal laser scanning microscopy (CLSM) with z-axis scanning. Multiple 3D stacks with average z-depths of ≈ 500 μm and interslice z-spacing of ≈ 1 μm were recorded at several random views. To evaluate the microgel volume fraction, the microscopy files were 3D reconstructed, thresholded, and smoothened to measure the percentage of the red fluorescent volume to the total volume.

Preparation of gelatin microparticle-based suspension medium: The gelatin microparticles were fabricated using a complex coacervation method adapted from literature[8]. A mix solution of 6.4 wt% gelatin type A (G1890, Sigma-Aldrich), 0.5 wt% Pluronic F-127 (P2443, Sigma-Aldrich), and 0.2 wt% gum arabic (51198, Sigma-Aldrich) in deionized water (DI water) was stirring and heating at 60 °C, followed by adding the same amount of ethanol. The beakers were sealed with parafilm to minimize evaporation and allowed to cool to room temperature (24–25 °C) while stirring at 400 rpm

overnight. The microgel-containing solution was centrifuged at 300 g for 5 min and the supernatant was discarded. The microgel pellets were washed with PBS thrice to remove residual ethanol and Pluronic F-127 at 4 °C. The microgel slurries were compacted by centrifugation at 1000 g and 4 °C for 5 min before being used for embedded 3D printing.

Rheological characterization: Rheological properties of MB bioink, suspension medium, and gelatin ink were measured using a rheometer (MCR301, Anton Paar) with a 25mm diameter cone plate geometry and gap size of 800 μm. The shear viscosity was measured at a ramped shear rate from 0 to 100 s^{-1} to evaluate the shear-thinning behavior. Temperature sweeps ranging from 4 ℃ to 37 ℃ (strain: 1%, frequency:1 Hz) were performed to evaluate the thermo- sensitive behavior. Strain sweeps ranging from 0.1% to 1000% (Temp: RT, frequency:1 Hz) were performed to examine the dynamic yielding properties. The storage (G') and loss moduli (G'') were measured with alternated low (1%) and high (300%) strains (1Hz, 100 s) for three cycles to evaluate the self-recovery properties.

3D direct bioprinting and embedded printing of MB bioink: 3D bioprinting of MB bioink in this study was performed using a commercial 3D bioprinter purchased from SunP Inc., China. All digital models including tube, bronchus, and heart were downloaded from the National Institutes of Health (NIH) 3D print exchange (https://3dprint.nih.gov/discover/3dpx-000452) or created in computer-aided design (CAD) software (SOLIDWORKS 2018, Dassault Systèmes). All 3D models were converted to STL format files and imported into the SunP software to generate G-Code instructions for the printer. The printing chamber was UV sterilized for 30 mins before printing. Cell-laden MB inks were loaded into 3 mL syringes (BD) and centrifuged at 1000 rpm for 10 s to remove any bubbles. For 3D direct printing, a printing speed of 5 mm/s and an extrusion rate of 1.8 μL/s were used at a temperature of 22 ℃. For embedded 3D printing, a printing speed of 3 mm/s and an extrusion rate of 0.38 μL/s were used at a temperature of 25 ℃. Upon print completion, the petri dish containing the printed construct was removed from the platform and exposed to visible light (405 nm, ~20 mW/cm^2) for 30 s on both sides. In this study, Carbopol-based and gelatin microparticle-based suspension media were used for embedded 3D printing. The removal of the Carbopol-based suspension medium was achieved by rinsing with PBS solution; while the removal of the gelatin microparticle-based suspension medium required an incubation at 37 ℃ for 30 min.

Sacrificial printing in MB ink-based suspension medium: The printing of sacrificial ink in MB-ink suspension medium was adapted from the SWIFT technique[16]. The MB bioink was loaded into the silicone molds or perfusion chambers, and further compacted via centrifugation at 100g. The 7.5% (w/v) gelatin solution was dissolved in PBS at 70°C and supplemented with 0.5% (v/v) red food coloring to enable visualization of printed ink. The freshly prepared sacrificial gelatin ink was loaded into a 3 mL plastic syringe that was mounted onto the 3D printer. The temperature of the printing

nozzle was maintained at 21°C for 20 min to induce gelation. For the bifurcated channels, the channel diameters were computed to ensure equivalent shear stress throughout the tissue matrix by following Murray's Law. The printing path, printing speed, and extrusion rate were controlled with G-code programmed with a custom-built MATLAB script. The filament diameter of each branch was tuned by changing the extrusion rate while maintaining a constant printing speed (e.g., 3 mm/s). The printing order of vascular geometry was carefully optimized to prevent the nozzle from translating through previously printed features.

SPIRIT printing: The SPIRIT technique included at least four separate printing processes as follows: i) A complex tissue construct such as the heart chamber was printed in the Carbopol or gelatin microparticles based suspension medium by embedded printing of MB bioink; ii) Upon the completion of heart chamber printing, 7.5% gelatin bioink was embedded printed in the freshly printed yet uncrosslinked heart chamber construct that served as a temporary suspension medium to generate free vascular network; iii) The printed heart chamber constructs made of MB bioink was rapidly stabilized by photocrosslinking; iv) The sacrificial suspension medium in (i) and sacrificial ink in (ii) were removed by temperature changing or repeated rinsing. We rendered each curvilinear line of the designed hierarchical vascular network as piecewise linear segments to generate G-code. For the first printing of MB bioink, a printing speed of 3 mm/s and an extrusion rate of 0.38 μL/s were used at a temperature of 25 ℃. For the second printing of gelatin bioink, a printing speed of 3 mm/s and an extrusion rate of 0.76 μL/s were used at a temperature of 24 ℃. Pluronic F127 ink (40wt%) was also used as sacrificial ink that was printed at 15℃during the second printing stage of SPIRIT. For the printing of a ventricle model, we used GelMA MB bioink embedded with neonatal rat ventricular cardiomyocytes at a density of 4×10^7 cells/ml. Printed ventricles were transferred to the incubator and supplemented with culture media containing 10% FBS.

Comparison between SPIRIT and multi-nozzle printing: A tubular construct (height of 12 mm, O.D. of 16 mm, I.D. of 10 mm) with a helical vascular network (width: 0.4 mm, pitch 2.0 mm) was used as an example to compare the fabrication time of SPIRIT and multi-nozzle printing. Carbopol-based suspension medium was used for both the SPIRIT and multi-nozzle printing strategies. For multi-nozzle printing, we sliced the tubular construct and helical vascular constructs separately and merged them together to guide the co-printing of both these two structures; however, the helical vascular construct was extruded continuously after the first printing of the tubular construct. We used a 3ml syringe from B&D Plastics with a 22G blunt needle (O.D. of 0.71 mm, I.D. of 0.41 mm). Layer height and line distance were both set at 0.4 mm. The default travel speed, normal printing speed, and extrusion rate were set at 10 mm/s, 3 mm/s, and 0.38 μL/s, respectively.

Printing fidelity analysis: The fidelity of printed filaments and constructs was analyzed by the structural similarity index (SSIM) via Python software. The images of printed samples were converted

into binary images using ImageJ software. These binary images were then segmented and compared against the binary images of theoretical design via SSIM in Python. The width of printed filaments and dimensions of printing constructs were measured using ImageJ software after calibration with a standard rule. SSIM values were analyzed with at least three printed samples for all experimental groups.

Mechanical testing: Cylinders with 8 mm circular diameter and 5 mm height were cast or embedded 3D printed, respectively. These samples were measured with a vernier caliper to determine their actual sizes before mechanical testing. Samples were loaded and compressed until rupture at the rate of 0.1 mm/s using a mechanical test instrument (Bose ElectroForce 3200, Bose Corp.). The elastic part (5% to 20% strain) of the stress-strain curve was selected to calculate the elastic modulus. For each condition, at least three samples were tested.

Cell viability assay: Cell viability of cell-laden microgels and printed structures was assessed using Calcein-AM/PI Double Staining Kit (C452, Dojindo Molecular Technologies). Briefly, the samples were incubated with 2 mM Calcein AM and 4.5 mM Propidium Iodide at 37 ℃ for 30~45 min and then visualized using a laser-scanning confocal microscope (FV3000, Olympus). Cell viability was analyzed by dividing live cell numbers by total cell numbers using ImageJ software.

Proliferation assay: Cell proliferation of 3D printed cell-laden structures was assessed using Cell Counting Kit-8 (CK04, Dojindo Molecular Technologies). Briefly, samples were transferred to one well of 6-well plates containing 2 mL medium supplemented with 200 μL of CCK-8 solution and incubated at 37℃. After 2 hours, 110 μL of the supernatant was transferred to a 96-well plate. This absorbance proportional to the number of living cells was measured at 450 nm using a microplate reader (Multiskan FC Microplate photometer, Thermo Scientific). For each condition, at least four samples were tested.

Fluorescence-activated cell sorting (FACS) analysis: Human iPSCs were first dissociated by Gentle Cell Dissociation Reagent (STEMCELL Technologies), fixed by 4% paraformaldehyde (PFA), and permeabilized by 0.1% Triton X-100 solution with saponin at room temperature. Primary anti-Nanog and anti-Oct4 antibodies were 1: 50 diluted in FACS buffer (DPBS with 2% FBS). Human iPSCs were incubated with primary antibodies at room temperature for 30 min and detected by Alexa Fluor® 488-conjugated and 594-conjugated secondary antibodies. The FACS analysis was performed by FACSAria™ Fusion flow cytometer (BD).

Immunofluorescence staining: For 3D printed constructs with hiPSCs, the samples were removed from the culture medium and washed with PBS three times. The washed samples were then fixed by 4% PFA, permeabilized by 0.1% Triton X-100 (T8787, Sigma), and blocked with 10% donkey serum albumin in PBST solution (0.1% Tween in PBS) for 1 hour at room temperature. The samples were incubated with primary antibodies against Nanog (1:500, ab173368, Abcam) and Oct4 (1:500, ab173368, Abcam) at 4℃ overnight. Subsequently, the samples were repeatedly rinsed with

PBS to remove unconjugated primary antibodies, followed by incubation using Alexa Fluor 488 goat anti-mouse (1:300, JAC-115-545-003, Jackson) for Nanog and Alexa Fluor 594 goat anti-rabbit (1:300, JAC-111-585-144, Jackson) for Oct4 at room temperature for 1 hour. Finally, the samples were counterstained with 4′,6-diamidino-2-phenylindole (DAPI, ab285390, Abcam) and visualized using a laser-scanning confocal microscope (FV3000, Olympus). For the immunostaining of cardiac tissues, primary antibodies including anti-sarcomeric α-actinin (1:200, ab9465, Abcam) and anti-cardiac troponin T (cTnT, 1:200, ab8295, Abcam) were used.

Perfusion of SPIRIT tissue constructs: The ventricle model was first placed on a supporting mold with the same curvature that was printed with transparent photosensitive resin. The inlet and outlet were connected with two stainless tubes and further sealed with GelMA hydrogel precursor, followed by UV curing. Next, the printed constructs were maintained at 37℃, where the sacrificial gelatin template (stained with red dye) was molten, and an injection pump (Langer Instruments Inc.) was used to introduce fluid media that evacuates the molten gelatin at a perfusion rate of 5 ml/hr. The perfusion process lasted at least 30 min to ensure the removal of all gelatin, which leaves behind transparent open channels. Later, PBS solution containing red or blue dye was perfused into the channels at a perfusion rate of 1.5~2.5 ml/hr smoothly.

Micro-computed X-ray tomography (μCT) scan: For measuring the fidelity of SPIRIT printing, 3D gauging of printed ventricles with complex vascular geometry was performed. After SPIRIT printing and photo-crosslinking, the container with the printed constructs was placed at 4℃ for 60 minutes before μCT scanning. Scans were performed on a desktop μCT machine (Skyscan 1272, Bruker, Belgium) with 10 μm voxel resolution. The 3D reconstruction was performed using Materialise Mimics software from the raw files and the resulting volumes were further processed to remove excess noise. The data was then converted to a surface STL file, which was overlaid with the volumetric 3D digital template using Magics software. Quantification of surface deviation between the scan and print template was performed to generate a heatmap of overprinted and under-printed regions.

Oxygen transport simulation: To determine the effect of vascular networks on cell viability, we performed an oxygen transport simulation based on the hypothesis that the cells and microgels were uniformly distributed within the printed constructs. We did not consider cell proliferation nor the influence of HUVEC coverage on channel permeability. The oxygen consumption of cells residing in the tissue matrix was characterized by the Michaelis-Menten Kinetics[31]. We defined the hypoxia region as oxygen concentration below 14 mmol, which could be detected by pimonidazole immunostaining. The incompressible Navier-Stokes model for Newtonian flow (constant viscosity) was employed to compute the flow velocity (equation 1).

$$\rho_m \cdot \frac{\partial v}{\partial t} = -\nabla P + \mu \cdot \Delta v + \rho_m \cdot g \quad (1)$$

In which, the density (ρ_m) and viscosity (μ) of the culture medium were extracted from the literature[10], and flow velocity (v) was set as 50 μL/min.

In domain I of the vascular network, oxygen transport was assumed to occur via both convection and diffusion, thus the governing equation for oxygen transport can be written as (equation 2).

$$\frac{\partial C}{\partial t} = -(\nabla C \cdot v) + \nabla \cdot (D_m \cdot \nabla C) \quad (2)$$

In which, oxygen diffusion coefficient (D_m) in culture medium was extracted from the literature[39].

In domain II of MB bioink where cells resided, oxygen transport is assumed to occur only via diffusion. The governing equation for the oxygen profile in domain II can be written as (equation 3).

$$\frac{\partial C}{\partial t} = \nabla \cdot (D_{GelMA} \cdot \nabla C) - \rho_c \cdot \frac{V_{O_2\,max} \cdot C}{K_m + C} \quad (3)$$

In which, the effective oxygen diffusion coefficient in the GelMA hydrogel (D_{GelMA}), cell density (ρ_c), and maximum uptake rate ($V_{O_2\,max}$) and Michaelis-Menten constant (K_m) of oxygen were extracted from the literature[40].

Calcium Transient Measurement: Electrophysiology of the printed ventricles was analyzed using calcium imaging. Printed ventricles were washed with Tyrode's solution to remove excess media and further incubated in Tyrode's solution containing 10 μM Fluo-4 acetoxymethyl ester (Fluo-4 AM, F312, Dojindo Laboratories) for 60 min at 37 ℃, followed by washing with Tyrode's salt solution to remove unbound dye. For imaging, the printed ventricles from spontaneous contractions were maintained in Tyrode's solution at 37 ℃ using a custom-built heated stage. Calcium transients in printed ventricles were recorded at a frame rate of 10 Hz with 20 ms exposure time using a DMi8 fluorescence microscope (Leica, Wetzlar). The acquired data was post-processed with custom MATLAB code. We generated the calcium traces by subtracting the fluorescence signals of beating sites with background signals of nonactive regions and normalizing them against the baseline intensity (F/F0).

Statistical analysis: All the experimental data were analyzed from at least three parallel samples, and expressed as mean ± standard deviation. Statistically significant differences between experimental groups were determined by one-way or two-way analysis of variance (ANOVA) using the Graph Pad Prism software (version 9.0) for Windows. Post hoc pairwise analysis was done with the Tukey HSD test. P-values below 0.05 were considered significant for all statistical tests.

Acknowledgments

We thank Jingjing Wang and Yue Sun at Cell Biology Facility, Center of Biomedical Analysis, Tsinghua University for their help with confocal microscopy. This work was funded by the National Natural Science Foundation of China (Grant No. U21A20394), the new faculty start-up Funding provided by Tsinghua University (53330200321), the National Key Research and Development Program of China (2018YFA0703004), and the China Postdoctoral Science Foundation (2021TQ0184).

Competing interests:

The authors declare that they have no competing interests.

Data and materials availability:

All data needed to evaluate the conclusions in the paper are present in the paper and/or the Supplementary Materials.

Received: ((will be filled in by the editorial staff))
Revised: ((will be filled in by the editorial staff))
Published online: ((will be filled in by the editorial staff))

References:

[1] S. V. Murphy, A. Atala, *Nat. Biotechnol.* **2014**, 32, 773.

[2] Y. Fang, Y. Guo, T. Liu, R. Xu, S. Mao, X. Mo, T. Zhang, L. Ouyang, Z. Xiong, W. Sun, *Chinese Journal of Mechanical Engineering: Additive Manufacturing Frontiers* **2022**, *1*, 100011.

[3] J. Cheng, F. Lin, H. Liu, Y. Yan, X. Wang, R. Zhang, Z. Xiong, *ASME. J. Manuf. Sci. Eng.* **2008**, 130, 021014.

[4] P. D. Dalton, T. B. F. Woodfield, V. Mironov, J. Groll, *Adv. Sci.* **2020**, 7, 1902953.

[5] H. W. Kang, S. J. Lee, I. K. Ko, C. Kengla, J. J. Yoo, A. Atala, *Nat. Biotechnol.* **2016**, 34, 312.

[6] A. McCormack, C. B. Highley, N. R. Leslie, F. Melchels, *Trends Biotechnol.* **2020**, 38, 584.

[7] T. Bhattacharjee, S. M. Zehnder, K. G. Rowe, S. Jain, R. M. Nixon, W. G. Sawyer, T. E. Angelini, *Sci. Adv.* **2015**, 1, e1500655.

[8] A. Lee, A. R. Hudson, D. J. Shiwarski, J. W. Tashman, T. J. Hinton, S. Yerneni, J. M. Bliley, P. G. Campbell, A. W. Feinberg, *Science* **2019**, 365, 482.

[9] Y. Fang, W. Sun, T. Zhang, Z. Xiong, *Biomaterials* **2022**, 280, 121298.

[10] Y. Fang, L. Ouyang, T. Zhang, C. Wang, B. Lu, W. Sun, *Adv. Healthc. Mater.* **2020**, 9, 2000782.

[11] D. B. Kolesky, K. A. Homan, M. A. Skylar-Scott, J. A. Lewis, *Proceedings of the National Academy of Sciences* **2016**, 113, 3179.

[12] L. Ouyang, J. P. K. Armstrong, Q. Chen, Y. Lin, M. M. Stevens, *Adv. Funct. Mater.* **2020**, 30, 1908349.

[13] N. Noor, A. Shapira, R. Edri, I. Gal, L. Wertheim, T. Dvir, *Adv. Sci.* **2019**, 6, 1900344.

[14] Y. Gu, A. Forget, V. P. Shastri, *Adv. Sci.* **2021**, 2103469.

[15] W. Wu, A. DeConinck, J. A. Lewis, *Adv. Mater.* **2011**, 23, H178.

[16] M. A. Skylar-Scott, S. G. M. Uzel, L. L. Nam, J. H. Ahrens, R. L. Truby, S. Damaraju, J. A. Lewis, *Sci. Adv.* **2019**, 5, w2459.

[17] Y. Fang, Y. Guo, M. Ji, B. Li, Y. Guo, J. Zhu, T. Zhang, Z. Xiong, *Adv. Funct. Mater*. **2022**, 32, 2109810.

[18] J. Wang, S. Hahn, E. Amstad, N. Vogel, *Adv. Mater.* **2022**, 34, 2107338.

[19] X. Liu, J. Tao, J. Liu, X. Xu, J. Zhang, Y. Huang, Y. Chen, J. Zhang, D. Y. B. Deng, M. Gou, Y. Wei, *ACS Appl. Mater. Inter.* **2019**, 11, 12209.

[20] M. Xie, Q. Gao, H. Zhao, J. Nie, Z. Fu, H. Wang, L. Chen, L. Shao, J. Fu, Z. Chen, Y. He, *Small* **2019**, 15, 1804216.

[21] C. B. Highley, K. H. Song, A. C. Daly, J. A. Burdick, *Adv. Sci.* **2019**, 6, 1801076.

[22] H. Zhang, Y. Cong, A. R. Osi, Y. Zhou, F. Huang, R. P. Zaccaria, J. Chen, R. Wang, J. Fu, *Adv. Funct. Mater.* **2020**, 30, 1910573.

[23] X. L. Yang, L. Pabon, C. E. Murry, *Circ. Res.* **2014**, 114, 511.

[24] D. M. Headen, G. Aubry, H. Lu, A. J. García, *Adv. Mater.* **2014**, 26, 3003.

[25] M. E. Kupfer, W. Lin, V. Ravikumar, K. Qiu, L. Wang, L. Gao, D. B. Bhuiyan, M. Lenz, J. Ai, R. R. Mahutga, D. Townsend, J. Zhang, M. C. McAlpine, E. G. Tolkacheva, B. M. Ogle, *Circ. Res.* **2020**, 127, 207.

[26] A. K. Grosskopf, R. L. Truby, H. Kim, A. Perazzo, J. A. Lewis, H. A. Stone, *ACS Appl. Mater. Inter.* **2018**, 10, 23353.

[27] T. J. Hinton, Q. Jallerat, R. N. Palchesko, J. H. Park, M. S. Grodzicki, H. Shue, M. H. Ramadan, A. R. Hudson, A. W. Feinberg, *Sci. Adv.* **2015**, 1, e1500758.

[28] M. E. Prendergast, J. A. Burdick, *Adv. Healthc. Mater.* **2022**, 11, 2101679.

[29] L. Ouyang, J. P. K. Armstrong, Y. Lin, J. P. Wojciechowski, C. Lee-Reeves, D. Hachim, K. Zhou, J. A. Burdick, M. M. Stevens, *Sci. Adv.* **2020**, 6, c5529.

[30] W. Cheng, J. Zhang, J. Liu, Z. Yu, *View* **2020**, 1, 20200060.

[31] J. Lee, S. Mehrotra, E. Zare Eelanjegh, R. O. Rodrigues, A. Akbarinejad, D. Ge, L. Amato, K. Kiaee, Y. Fang, A. Rosenkranz, W. Keung, B. B. Mandal, R. A. Li, T. Zhang, H. Lee, M. R. Dokmeci, Y. S. Zhang, A. Khademhosseini, S. R. Shin, *Small* **2021**, 17, 2004258.

[32] L. Shao, Q. Gao, C. Xie, J. Fu, M. Xiang, Y. He, *Biofabrication* **2020**, 12, 35014.

[33] L. A. MacQueen, S. P. Sheehy, C. O. Chantre, J. F. Zimmerman, F. S. Pasqualini, X. Liu, J. A. Goss, P. H. Campbell, G. M. Gonzalez, S. Park, A. K. Capulli, J. P. Ferrier, T. F. Kosar, L. Mahadevan, W. T. Pu, K. K. Parker, *Nat. Biomed. Eng.* **2018**, 2, 930.

[34] J. S. Miller, K. R. Stevens, M. T. Yang, B. M. Baker, D. T. Nguyen, D. M. Cohen, E. Toro, A. A. Chen, P. A. Galie, X. Yu, R. Chaturvedi, S. N. Bhatia, C. S. Chen, *Nat. Mater.* **2012**, 11, 768.

[35] H. C. Ott, T. S. Matthiesen, S. Goh, L. D. Black, S. M. Kren, T. I. Netoff, D. A. Taylor, *Nat. Med.* **2008**, 14, 213.

[36] I. S. Kinstlinger, S. H. Saxton, G. A. Calderon, K. V. Ruiz, D. R. Yalacki, P. R. Deme, J. E. Rosenkrantz, J. D. Louis-Rosenberg, F. Johansson, K. D. Janson, D. W. Sazer, S. S. Panchavati, K. Bissig, K. R. Stevens, J. S. Miller, *Nat. Biomed. Eng.* **2020**, *4*, 916.

[37] C. B. Highley, C. B. Rodell, J. A. Burdick, *Adv. Mater.* **2015**, 27, 5075.

[38] J. H. Ahrens, S. G. M. Uzel, M. Skylar Scott, M. M. Mata, A. Lu, K. T. Kroll, J. A. Lewis, *Adv. Mater.* **2022**, 2200217.

[39] T. Kang, J. M. Hong, J. W. Jung, J. J. Yoo, D. Cho, *Langmuir* **2013**, 29, 701.

[40] T. Fiedler, I. V. Belova, G. E. Murch, G. Poologasundarampillai, J. R. Jones, J. A. Roether, A. R. Boccaccini, *Journal of Materials Science: Materials in Medicine* **2014**, 25, 2573.

Figures

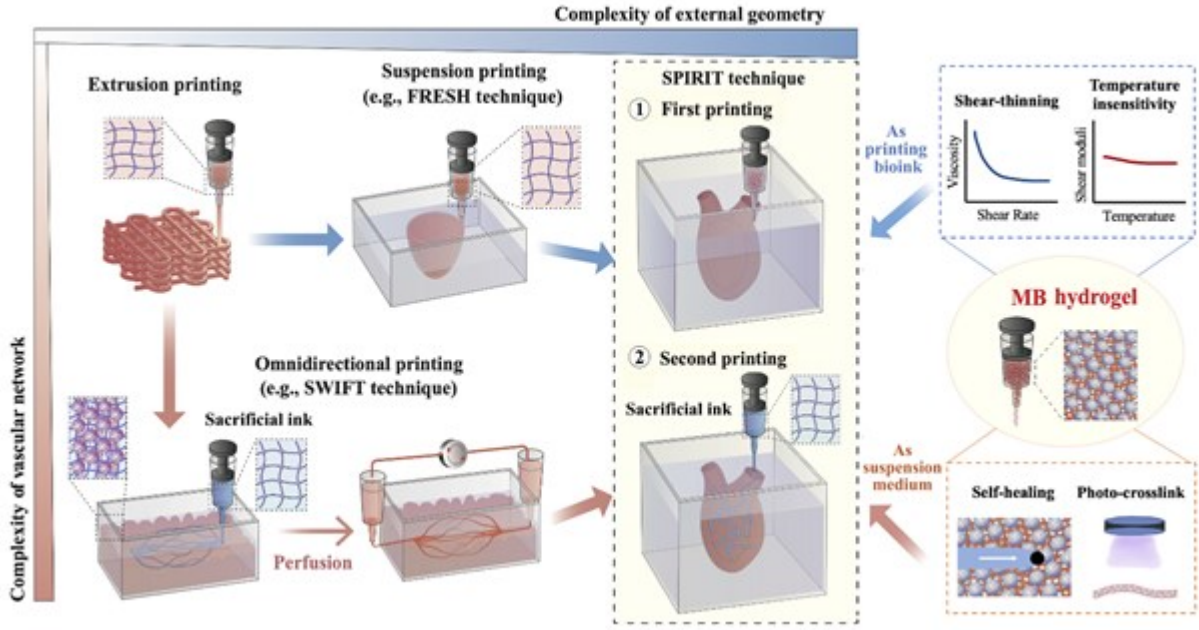

Figure 1. Expanding extrusion bioprinting capability by sequential printing in reversible ink template (SPIRIT) strategy. Owing to the self-thinning and self-healing behavior, the microgel-based biphasic (MB) hydrogel can be used as both an excellent bioink for embedded 3D printing and serve as a suspension medium that supports embedded 3D printing. The SPIRIT strategy enables the fabrication of tissue and organ constructs with both the complex external geometries and vascular structures by sequential printing of MB bioink and sacrificial bioink.

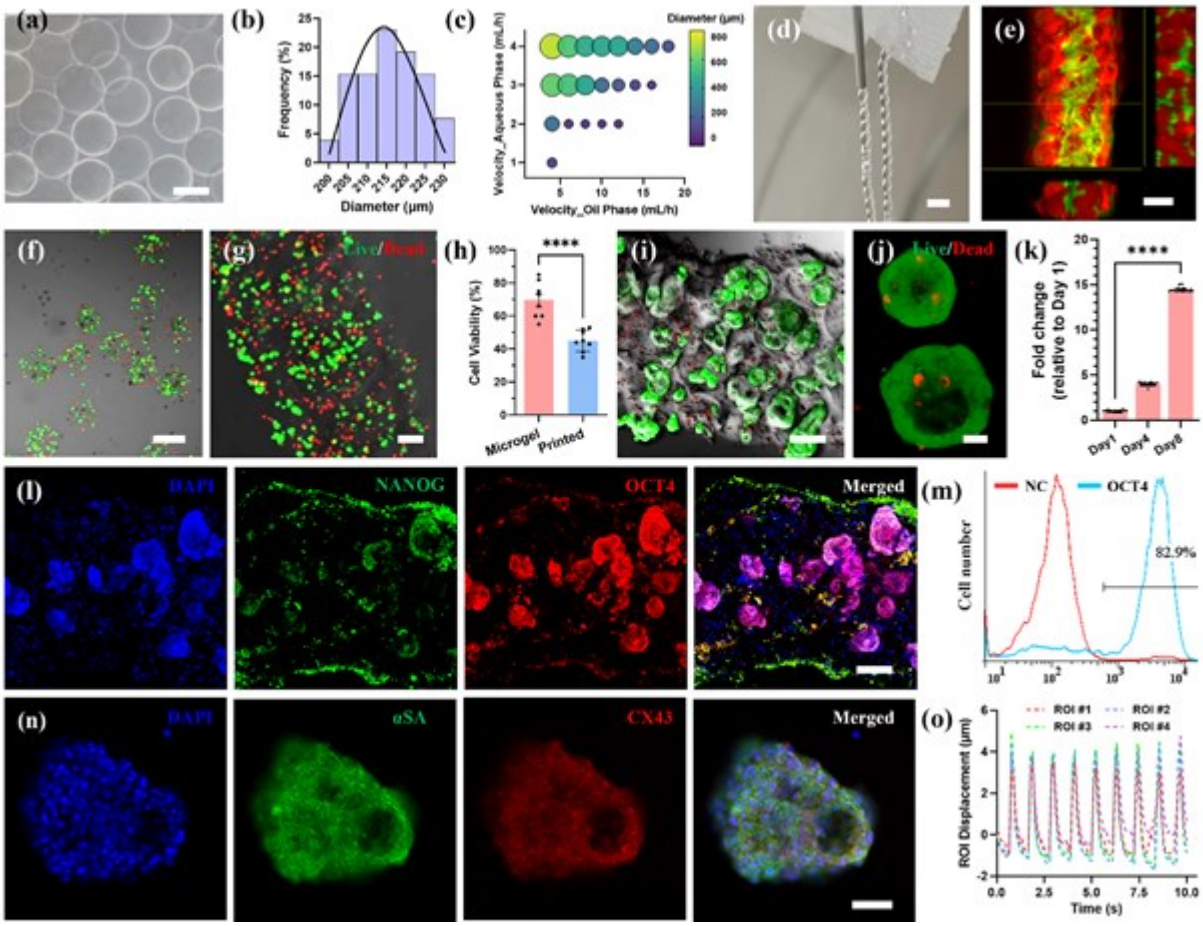

Figure 2. Characterization and 3D printing of cell-laden MB bioink. (a) Microgel generation by microfluidic devices. (b) A histogram showing the diameter distribution of alginate/gelatin microgels. The solid black indicates the fitted curve of the diameter distribution. (c) Microgel diameters could be tuned by changing the flow velocity of the aqueous phase and oil phase. (d) Filament extrusion of MB bioink. (e) Fluorescent image of 3D printed filament (microgel, red; second hydrogel, green) showing the microgels were densely packed within a second hydrogel. (f) Live/Dead staining (Calcein AM, green; PI, red) of hiPSCs-laden alginate/gelatin composite microgels. (g) Live/Dead staining of 3D printed filament using hiPSCs-laden MB ink on day 0. (h) Cell viability before and after printing. The student's t-test was used to analyze the data, *$p < 0.05$. (i) Live/Dead staining of 3D printed filament using hiPSCs-laden MB ink on day 7. (j) Magnified view of (i) showing the morphology of EBs. (k) Proliferation rates of hiPSCs within MB bioink during culture. (l) Immunofluorescence images of EBs stained with Oct4, Nanog, and DAPI. (m) Quantification of 3D dissociated cells marked with Oct4 and Nanog by using flow cytometry. (n) Representative immunofluorescence (alpha-SA, green; cx43, red; DAPI, blue) of EBs on day 21 showing directed cardiomyocyte differentiation. (o) Representative contraction profiles of cardiac organoids. Scale bars in (a) 200 μm; (d) 1 mm; (e-f) 200 μm; (g) 100 μm; (i) 100 μm; (j) 20 μm; (l) 100 μm; (n) 50 μm.

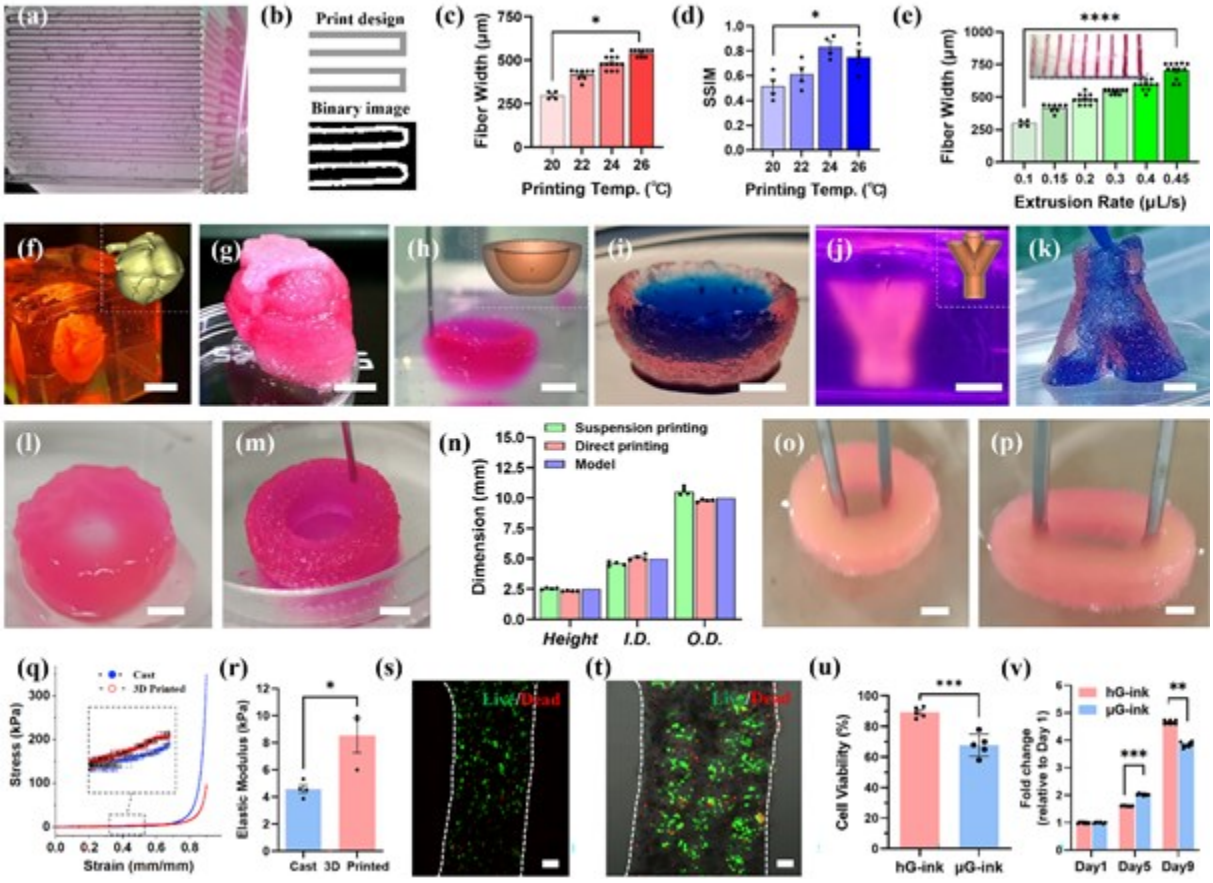

Figure 3. Embedded 3D printing of MB bioink for complex tissue engineering. (a) Representative image of the printed filaments using MB bioink in the Carbopol-based suspension medium. (b) Custom G-code design of the printed filaments and a binary image isolated from them. (c) The average filament width at varied printing temperatures. (d) The structural similarity index measure (SSIM) is used as a metric to measure the similarity between the printed filaments and their print design. (e) Measurement of filament widths printed at varied extrusion rates ranging between 0.1 μL/s and 0.45 μL/s. *P< 0.05, **P< 0.001, one-way ANOVA with Tukey post-hoc test. (f) 3D printed full heart model in a Carbopol-based suspension medium (inset: 3D CAD model). (g) 3D printed heart model after removing from suspension medium. (h) 3D printed open chamber model in a Carbopol-based suspension medium (inset: 3D CAD model). (i) The printed open chamber contained blue ink without leakage. (j) 3D printed bronchus model in a Carbopol-based suspension medium (inset: 3D CAD model). (k) The printed bronchus was perfused with blue ink. (l) The tubular structure (O.D.: 10 mm, height: 2.5 mm) by embedded printing strategy after exacting from the Carbopol-based suspension medium. (m) The tubular structure with the same dimensionality by direct printing strategy. (n) Measured height, I.D., and O.D. of 3D printed tubular structures in (k,l). (o-p) A embedded printed tubular structure under cyclic stretching. (q-r) Representative stress-strain curves of cast and 3D printed cylinders at uniaxial compression test (q) and (r) elastic moduli. (s-t) Live/Dead fluorescent staining of 3D printed filaments using HepG2-laden GelMA hydrogel bioink (s) and

HepG2-laden MB bioink (t), respectively. (u) Viability of hepatic cells within GelMA bioink and MB bioink, respectively. (v) Normalized proliferation rates of hepatic cells within GelMA bioink and MB bioink, respectively. In subfigures (u-v), hG-ink denotes hydrogel-based bioink while μG-ink denotes microgel-based biphasic (i.e., MB) bioink. The student's t-test was used to analyze the data, *p < 0.05. Scale bars in (f) 10 mm; (g-i) 5 mm; (j) 4 mm; (k-m) 2 mm; (o-p) 2 mm; (s-t) 100 μm.

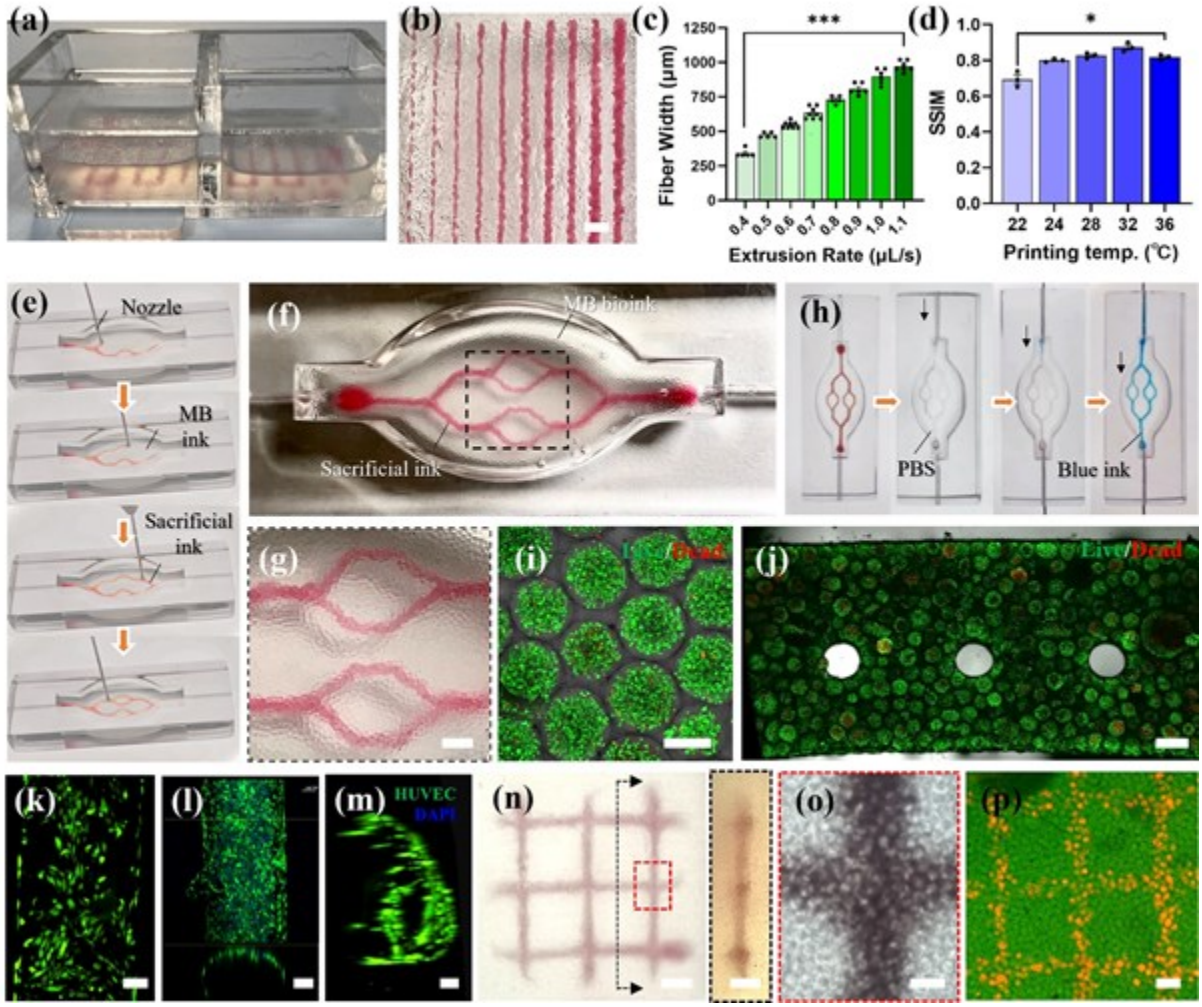

Figure 4. MB bioink serves as a suspension medium for embedded printing. (a) Representative image of embedded printing using an MB bioink-based suspension medium. (b) The filaments were printed at varied extrusion rates. (c) The filament width as a function of extrusion rate. (d) The SSIM comparison at different printing temperatures. *P< 0.05, **P< 0.001, one-way ANOVA with Tukey post-hoc test. (e) An image sequence showing the embedded printing of a branched vascular network within the MB bioink-based suspension medium. (f,g) The optical images of the 3D printed branched structures. (g) Magnified view of (f). (h) An image sequence showing sacrificial ink (red) evacuation upon incubation, and culture medium perfusion containing blue dye after connecting with a syringe pump. (i) Live/Dead fluorescent staining of MB bioink loaded with HepG2 cells at a density of 4×10^7

cells/ml. (j) The fluorescent image of cell viability stained at the cross-section through the printed tissue. (k) Green fluorescent-labeled HUVEC adhesion and spreading on the channel wall on day 3. (l) Formation of a monolayer of a HUVEC endothelium on day 7. HUVECs invasion into the surrounding matrix was observed. (m) 3D reconstructed microvessel formed by endothelial cell self-assembly. (n) A mesh-like structure by printing MB bioink (stained with red dye) within the suspension medium consisting of MB bioink. Left, vertical view; right, cross-section view. (o) The optical image of the printed structure illustrates that the bioink and suspension medium both consist of microgels. (p) The fluorescent image of printed meshes (microgels, red) within the suspension medium (microgels, green). Scale bars in (b) 2 mm; (g) 1 mm; (h) 200 μm; (j) 500 μm; (k-l) 100 μm; (m) 50 μm; (n) 2 mm; (o-p) 500 μm.

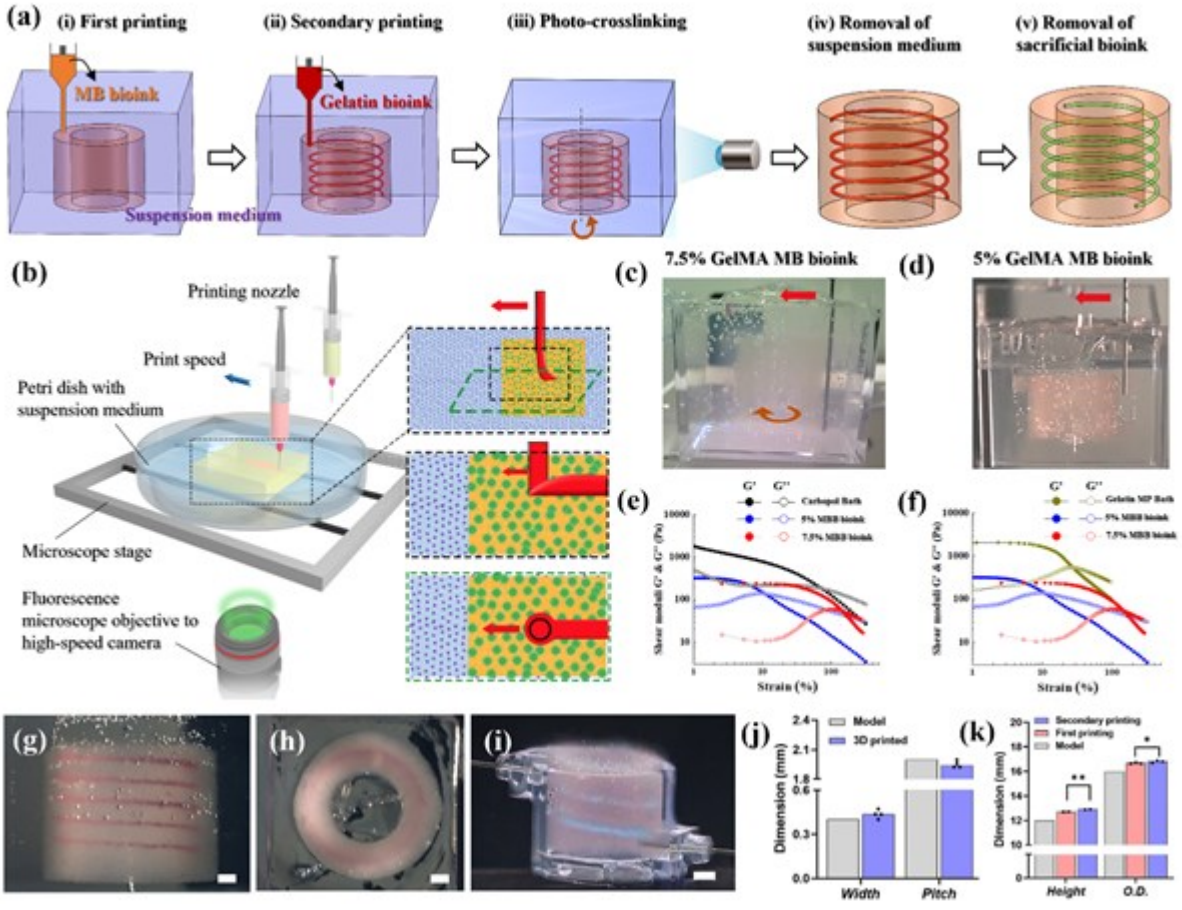

Figure 5. Sequential printing in reversible ink template strategy by using MB bioink. (a) Schematic illustration of SPIRIT printing which includes typical five separate printing processes: i) first printing; ii) second printing; iii) photocrosslinking; iv) removal of suspension medium; v) removal of sacrificial ink. (b) Extrusion of MB bioink into the Carbopol-based suspension medium was assessed via in situ monitoring. (c,d) SPIRIT printing of a tubular structure embedded with a helical vascular network using 7.5% GelMA MB bioink (c) and 5% GelMA MB bioink (d),

respectively. (e) Strain sweeps of Carbopol-based suspension medium, 7.5% and 5% GelMA MB bioink, respectively. (f) Strain sweeps of gelatin microparticles based suspension medium, 7.5% and 5% GelMA MB bioink, respectively. (g,h) The optical images of printed tubular construct embedded with a gelatin-based helical structure (stained with red dye) at the front view (g) and top view (h). (i) Perfusion of the printed tubular construct through the helical channels. (j) Measured widths and pitches of the printed helical channels. (k) Measured heights and O.D. values of 3D printed tubular structures upon the completion of first printing and secondary printing, respectively. The student's t-test was used to analyze the data, *$p < 0.05$. Scale bars in (g,h) 2 mm; (i) 4 mm.

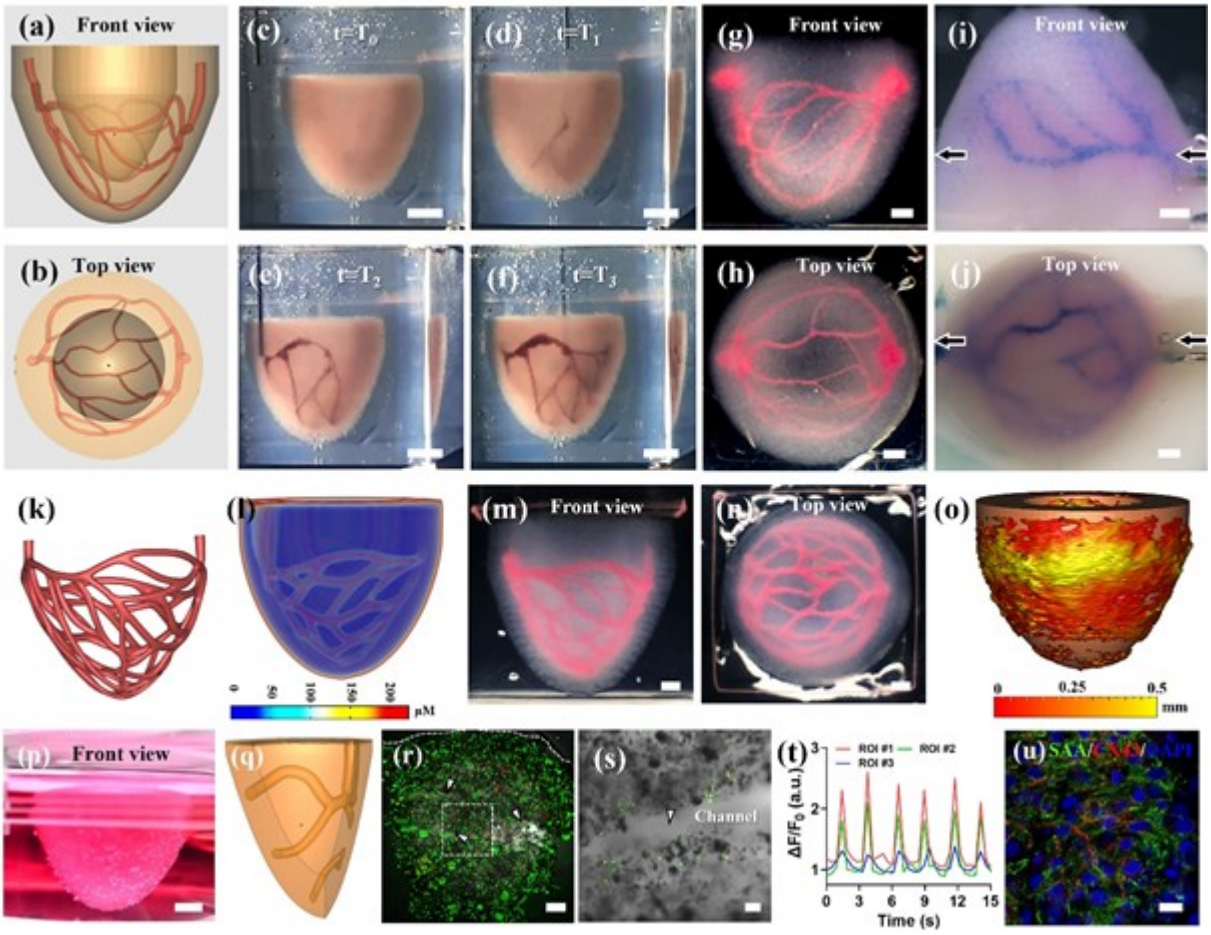

Figure 6. Perfusable ventricle constructs fabricated by SPIRIT. (a,b) 3D design of the hierarchical vascular network within a ventricle construct (f: front view; g: top view). (c) The optical image

showing the first printing process of the ventricle using MB bioink in Carbopol-based suspension medium. (d-f) An image sequence showing the second printing process of a hierarchical vascular network by extruding gelatin ink into the printed ventricle, which served as a temporary suspension medium. (g-h) The optical images showing a 3D printed ventricle with a hierarchical vascular network (containing red dye) at the front view (g) and top view (h). (i,j) The optical images showing the perfusion of the vascular networks within the printed ventricle construct (top: front view; bottom: top view). (k) 3D design of a dendritic vascular network with higher density. (l) Simulation of oxygen distribution within the ventricle containing a dendritic vascular network at a cell density of 5×10^6 cells/ml (front view). (m,n) The optical images showing a 3D printed ventricle with a densely packed vascular network (containing red dye) at the front view (m) and top view (n). (o) A heat map showing the geometric difference between the template (orange color) and the final print structure (red and yellow color). (p) The optical image showing the printed ventricle consisting of NRVCs-laden MB bioink. (q) Illustration of cardiac patch cut from the printed ventricle. (r) Live/Dead fluorescent staining of a large piece of the printed tissue. (s) High magnification image at a single z-depth in (r) showing the distribution of vascular channels (white arrows pointing to the channels). (t) Calcium transients of printed cardiac tissues on day 10. (u) Immunostaining of sarcomeric alpha-actinin (SAA, green), connexin 43 (cx43, red), and DAPI (blue) on printed cardiac tissues on day 15. Scale bars in (c-f) 5 mm; (g-j) 2 mm; (l-m) 2 mm; (p) 2 mm; (r) 1 mm; (s) 100 μm; (u) 10 μm.

Table of Contents (ToC)

Expanding Embedded 3D Bioprinting Capability for Engineering Complex Organs with Freeform Vascular Networks

Yongcong Fang[#], Yihan Guo, Bingyan Wu, Zibo Liu, Min Ye, Yuanyuan Xu, Mengke Ji, Li Chen, Bingchuan Lu, Kaiji Nie, Zixuan Wang, Jianbin Luo, Ting Zhang, Wei Sun, Zhuo Xiong[*]

In vitro replication of the external geometry of specific organs and their internal structures such as blood vessels simultaneously remains one of the greatest challenges in the biofabrication field. This study introduces a generalizable bioprinting strategy of sequential printing in a reversible ink template (SPIRIT) to address this limitation. Moreover, the SPIRIT technique has significantly reduced the printing time compared to the conventional multi-material bioprinting strategy.